Numerical Simulations of Island-Induced Circulations and Windward Katabatic Flow over the Guadeloupe Archipelago

Raphaël Cécé, Didier Bernard, Christophe D'alexis, Jean-François Dorville

Numerical Simulations of Island-Induced Circulations and Windward Katabatic Flow over the Guadeloupe Archipelago

RAPHAËL CÉCÉ, DIDIER BERNARD, AND CHRISTOPHE D'ALEXIS

Department of Physics, University of the French West Indies and French Guiana, Pointe-à-Pitre, Guadeloupe

JEAN-FRANÇOIS DORVILLE

Department of Physics, University of West Indies, Kingston, Jamaica

(Manuscript received 8 April 2013, in final form 18 September 2013)

ABSTRACT

This article deals with the first high-resolution numerical modeling of the weather over the small and high islands of the Guadeloupe archipelago. Its main goal is to analyze the mechanisms that drive local-scale airflow circulations over this archipelago, using the 1-km Weather Research and Forecasting Model (WRF). Three meteorological situations corresponding to weak trade winds (WTW), medium trade winds (MTW), and strong trade winds (STW) have been selected and are linked with local Froude number values of 0.21, 0.41, and 0.82, respectively. For these three weather types, simulated typical meteorological variables present a good agreement with observational data at several locations. The 48-h simulations allow the completion of the previous coarse observational descriptions that did not include a map of the wind, skin temperature, cloud cover, and sensible heat flux for the whole archipelago. The expected local wind regime areas (windward, inland, and leeward) are retrieved in the model outputs, including the predominance of thermal and orographic effects over Grande-Terre Island and Basse-Terre Island, respectively. Under STW, the convection is inhibited and the local circulations are driven by the orography. In the case of WTW, the model simulates well a katabatic wind, inducing cold nocturnal reversed flow on the windward coast of Basse-Terre. This circulation, opposing the trade winds, extends to the sea and Grande-Terre Island. This flow has a maximum wind speed of 4.7 m s^{-1}. This particular flow occurring in the most densely populated area produces an important nocturnal pollution period due to industrial sources (the diesel power plants of the archipelago).

1. Introduction

Many authors have shown that strong radiative and high topography forcings may induce local circulations over tropical islands. Mechanical effects of islands on the steady trade winds is characterized by the local Froude number Fr_m which is defined by (U/Nh_m), where U is the wind speed, h_m is the height of the mountain, and N is the buoyancy frequency. The literature dealing with this subject is generally concerned with one of three types of island: large (i.e., $\mathrm{Fr}_m \geq 1$, width >50 km), high (i.e., $\mathrm{Fr}_m < 1$), or small (i.e., $\mathrm{Fr}_m \geq 1$, width ≤50 km).

Effects of large islands on synoptic winds have been examined for the Tiwi Islands (Oliphant et al. 2001) and Puerto Rico (Malkus 1955; Jury et al. 2009). Oliphant et al. (2001) showed that with a flat area of 8000 km^2, the Tiwi Islands generate their own thermal airflow regime associated with sea/land-breeze systems. The Weather Research and Forecasting Model (WRF) simulation over Puerto Rico (Jury et al. 2009), indicated how diurnal heating and orography act on the convective boundary layer structure and trade wind airstream. In general, high islands like the Hawaiian Islands (Smith and Grubiac 1993; Reisner and Smolarkiewicz 1994; Feng and Chen 1998; Yang and Chen 2005; Carlis et al. 2010; Nguyen et al. 2010), New Caledonia (Lefèvre et al. 2010), Reunion Island (Lesouëf et al. 2011), or Lesser Antilles islands like St. Vincent (Smith et al. 1997) and Dominica (Smith et al. 2012) would have mainly mechanical effects on the impinging airflow with in some cases thermal circulations occurring on the lee side. During the Dominica Experiment field campaign (DOMEX), Smith et al. (2012) observed that two types

Corresponding author address: Raphaël Cécé, Faculty of Sciences, Department of Physics, University of the French West Indies and French Guiana, Fouillole campus, Pointe-à-Pitre 97110, Guadeloupe. E-mail: raphael.cece@univ-ag.fr

DOI: 10.1175/MWR-D-13-00119.1

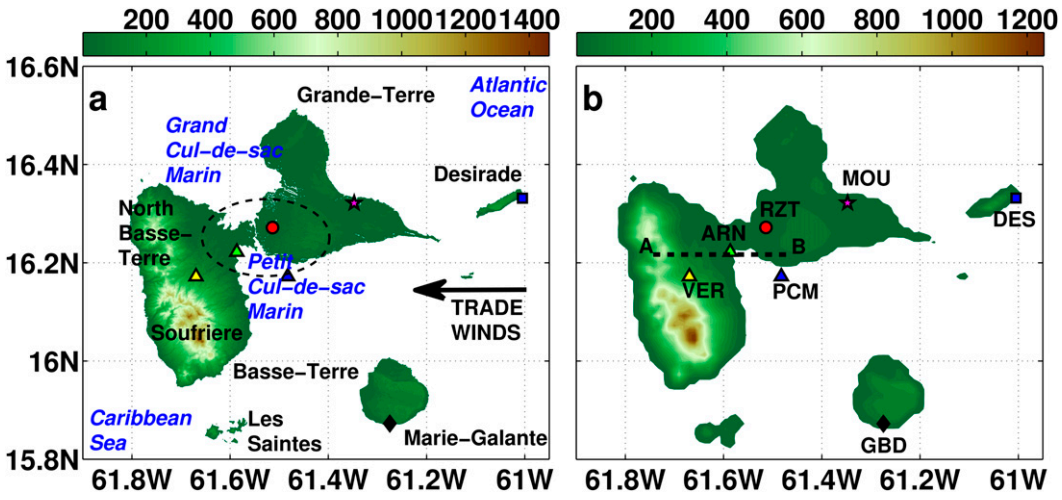

FIG. 1. Map of the Guadeloupe archipelago, including terrain height (m) and locations of five weather stations and two numerical points of study, respectively: Arnouville (ARN, green triangle), Raizet (RZT, red circle), Moule (MOU, magenta star), Désirade (DES, blue square), Grand-Bourg (GBD, black diamond), Vernou (VER, yellow triangle), and Petit Cul-de-sac Marin (PCM, blue triangle), VER and PCM are the two numerical stations. (a) IGN topography of 50-m resolution with black dashed ellipse indicating most densely populated area. (b) The model topography of 1-km resolution with a vertical cross section A–B.

of airflow patterns occur over the mountainous island of Dominica, depending on the trade wind intensity (i.e., under wind speed below $5\,m\,s^{-1}$ and above $8\,m\,s^{-1}$), anabatic flow, and plunging flow occur, respectively, over lee slopes. The thermal impacts of small islands on the marine boundary layer (MBL) have been analyzed observationally and numerically over the 40-km diameter Barbados Island (De Souza 1972; Mahrer and Pielke 1976) and over the 5-km-diameter Pacific island of Nauru (Savijrvi and Matthews 2004; Matthews et al. 2007). These studies showed that because of surface heating, small islands are able to generate their own circulations driven by convection.

The Guadeloupe archipelago with an area of $1600\,km^2$, is located in the Lesser Antilles at the limit between the Leeward and Windward Islands (16.15°N, 61.35°W). Guadeloupe includes two main islands (Fig. 1): Basse-Terre Island, a volcanic mountainous island with a complex topography that rises to 1467 m (the volcano of La Soufrière); and Grande-Terre, a sedimentary limestone tray island with low topography that rises to 135 m (separated from Basse-Terre by a narrow sea channel called Salt River). This narrow sea channel is bordered by two shallow sea areas: Le Petit Cul-de-sac Marin and Le Grand Cul-de-sac Marin, located in the south and north parts, respectively. Désirade, Marie-Galante, and Les Saintes are other smaller islands of the archipelago. The special feature of Guadeloupe is the combination of two types of island (Fig. 1): the high island of Basse-Terre ($Fr_m < 1$ and width ≤ 50 km) and the small, relatively flat island of Grande-Terre ($Fr_m > 1$ and width ≤ 50 km). In this article, observational data over Guadeloupe are extracted from four available French Met Office weather stations (Raizet, Désirade, Moule, and Grand-Bourg) and the Research Laboratory in Geosciences and Energy coastal weather station of Arnouville named as RZT, DES, MOU, GBD, and ARN, respectively (Fig. 1).

There are very few studies dealing with local circulations over Guadeloupe. On the basis of offshore observations and stations data, Bleuse and Bleuse (1997) presented some aspects of the wind over the archipelago. They defined three local wind regimes: the windward regime (i.e., steady synoptic winds blowing without nocturnal calm; DES and MOU, Fig. 1); the inland regime in the middle of the archipelago (i.e., land areas around the Grand Cul-de-Sac Marin and the Petit Cul-de-Sac Marin; ARN, RZT, GBD, Fig. 1), with, at night, the ground radiative cooling resulting in a calm in the lowest atmospheric layers; and the leeward regime (including the mountain regime), which is driven by local thermal and dynamical effects, and under which the wind is mostly weak and disturbed on the leeward side. Under weak synoptic winds, Bleuse and Bleuse (1997) observed few occurrences of light land breezes on the windward coast of Grande-Terre (MOU, Fig. 1). This coarse description of airflow circulations has been published in Brévignon (2003). D'Alexis (2011) has conducted a field experimental campaign to analyze microscale phenomena in the mangrove surface layer. From April 2007 to June 2008, the Research Laboratory in Geosciences

and Energy weather station recorded 1- and 20-Hz measurements at the coastal area of Arnouville (i.e., the windward side of Basse-Terre Island, ARN, Fig. 1). The 1-yr data recorded show that generally under weak to moderate trade winds, there are occurrences of low-level nocturnal reversed flow associated with a sudden fall of 2-m temperature. The location (i.e., a coastal area at the bottom of the windward slopes of the mountainous range), could suggest a katabatic wind and/or land breeze. Feng and Chen (1998) observationally analyzed the evolution of katabatic flow occurring on the windward side of the island of Hawaii under trade wind speeds on the order of $\sim$4–7 m s^{-1}.

To fill spatiotemporal data gaps over Guadeloupe, in particular over the most densely populated area (black dashed area, Fig. 1), it is necessary to go through numerical modeling. The present work is the first high-resolution numerical study of airflow circulations over this particular archipelago. The Advanced Research WRF version 3 (ARW-WRF V3; Skamarock et al. 2008) is used to simulate real cases of weak, medium, and strong trade winds linked with local Froude number values of 0.21, 0.41, and 0.82, respectively (with $U = 3$, 6, and 12 m s^{-1}; $N = 0.01$ s^{-1}; and $h_m = 1460$ m). The main purpose of this work is to better understand the thermal and dynamical impacts of Guadeloupe on synoptic wind flows. The hourly 1-km numerical results would allow us to analyze particular local scale phenomena such as the nocturnal reversed flow on the windward coast of Basse-Terre (D'Alexis et al. 2011). High-resolution simulated meteorological fields start to be applied to other problematics: atmospheric pollution in lower layers (Saharan and volcanic dusts, industrial aerosol particles, and gases), wind energy potential, and the evaluation of atmospheric and oceanic risks under hurricane threat (Cécé et al. 2013).

This paper is organized as follows. Section 2 includes the main factors forcing the local airflow circulations in Guadeloupe (i.e., the selected weather types, the expected orographic effects on an adiabatic flow, and the diurnal variability). The model configuration and evaluation are presented in section 3. Section 4 presents the analysis of the 1-km numerical results for the three weather types, including the specific reversed cold wind observed by D'Alexis et al. (2011). Section 5 concludes the study.

2. Main factors forcing the local airflow circulations in Guadeloupe

a. Selected weather types

Morvan (2011) defined a climatological classification of weather types in the Lesser Antilles and French Guiana. This *k*-means classification is based on 20 years of observations and the European Centre for Medium-Range Weather Forecasts (ECMWF) Interim Re-Analysis (ERA-Interim) fields: 850-hPa horizontal wind speed, 600-hPa vertical wind speed, 200-hPa horizontal wind speed divergence, MSL pressure, 2-m temperature, 925-hPa temperature, and 850-hPa wet-bulb potential temperature. To simulate and study local wind circulations around and above the Guadeloupe archipelago, three weather types have been chosen from this classification. They depend on the impinging flow velocity in conformity with the method presented by Lesouëf et al. (2011) and Smith et al. (2012). The weak trade winds (WTW), the medium trade winds (MTW), and the strong trade winds (STW) are associated with wind velocities of 3, 6, and 12 m s^{-1}, respectively. Following the Morvan (2011) classification, MTW is the most common weather type (60% of cases in the year). STW and WTW weather types each account for 10% of cases in the year. The remaining 20% of cases correspond with strong rainy disturbances (cold fronts, waves, cyclones, etc.).

To get observational data from the windward coast of Basse-Terre, studied days have been selected from the D'Alexis (2011) field campaign period. The dry transition month of December has been chosen because of the occurrence of the three weather types and the absence of strong synoptic disturbances. Following these criteria and the classification (Morvan 2011), three 48-h periods corresponding to WTW, STW, and MTW cases, respectively, are analyzed in the present study: 0600 UTC 3 December–0600 UTC 5 December 2007, 0600 UTC 14 December–0600 UTC 16 December 2007, and 0600 UTC 24 December–0600 UTC 26 December 2007 (with UTC corresponding to LT + 4). The troposphere stratification of these three periods is described by the 1200 UTC RZT (78897 TFFR) soundings. The soundings, extracted from the Wyoming data center (http://weather.uwyo.edu/upperair/sounding.html), are plotted for the first day of each weather type and four meteorological variables (Fig. 2). From bottom to the tropopause, the stratification includes coarsely: the nocturnal surface inversion layer, the subcloud layer, the cloud layer, the trade wind inversion layer, and the westerlies layer. For the three weather types, the dry potential temperature profiles are very close (Fig. 2a). In the case of WTW (blue circles, Fig. 2), the typical east wind direction in the surface layer is reversed. In section 2c, nocturnal reversed flows have been observed by D'Alexis et al. (2011) during weak to moderate winds on the windward coast of Basse-Terre Island. The sounding would suggest that this flow extends to Grande-Terre Island. The trade winds are found between 950 and 350 hPa with a north-northeast direction. Above, the westerlies layer is associated with a jet at 200 hPa.

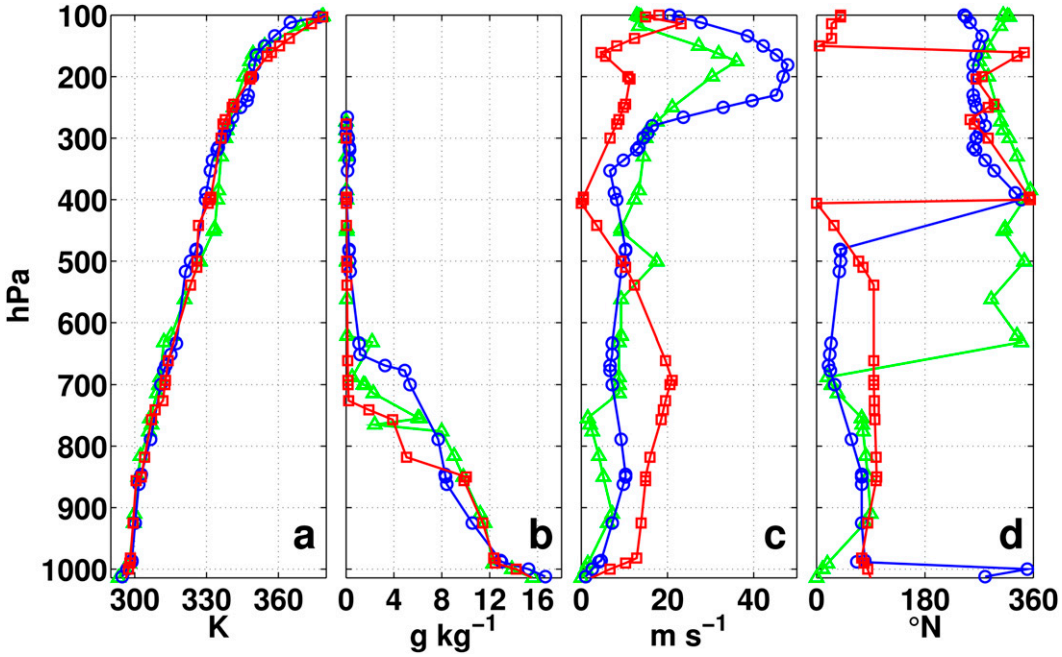

FIG. 2. Observed RZT 1200 UTC soundings for the three weather types: WTW (Fr_m = 0.21) 3 Dec 2007 (blue circles), MTW (Fr_m = 0.41) 24 Dec 2007 (green triangles), and STW (Fr_m = 0.82) 14 Dec 2007 (red squares): (a) dry potential temperature (K), (b) water vapor mixing ratio (g kg^{-1}), (c) wind speed (m s^{-1}), and (d) wind direction (°N).

In the case of MTW (green triangles, Fig. 2), the nocturnal surface layer conditions induce wind velocities lower than WTW ones (null to 1.5 m s^{-1}, Fig. 2c). The westerlies appear at 630 hPa. This is associated with the increase in wind speed (above 10 m s^{-1}) and the near-zero water vapor mixing ratio above this level. In the easterlies layer, the water vapor mixing ratio decreases by stages.

STW (red squares, Fig. 2) generate a shallow westerlies layer between 400 and 150 hPa (Fig. 2d). From bottom to top, we observe three parts: the easterlies (1000–400 hPa), the westerlies (400–150 hPa), and a north-northeast flow (at the tropopause). Wind speed reaches values well above 10 m s^{-1} between 1000 and 500 hPa (Fig. 2c).

We note that under MTW and WTW, the drying of the air mass is linked with the westerlies layer whereas it is not under STW. In the lowest layers, dynamical variables, wind speed, and direction present the major differences between the three weather types, whereas each dry potential temperature and water vapor mixing ratio are very close.

b. *Expected orographic effects on adiabatic flows*

The direction of the trade winds airflow is mostly perpendicular to the Basse-Terre mountain range (Fig. 1). The Basse-Terre mountain range can be divided into two parts: the south side comprises the volcanic highland of La Soufrière rising to 1467 m and the northside can be considered as a lower mountainous barrier with an average height of 500 m. Basse-Terre Island would have the most important local dynamical impacts on the steady airflow. Smith et al. (1997) observed on satellite images long straight wakes (300 km) in the lee of small windward islands (like St. Vincent with 20-km width and 1-km height). These wakes were characterized in the case of dense trade winds cumuli by a free cloud band and on the other hand by a thin row of cumulus clouds along their boundaries. This phenomenon also appears in some cases, on the satellite images of the lee of Basse-Terre Island.

As written by Lesouëf et al. (2011), the presence of an isolated island would disturb the uniform background flow and could produce various flow patterns, such as blocking on the windward side, Venturi effect on the laterals, and vortices in the lee. The flow may go above or around the island depending on vertical stability, maximum obstacle elevation, and speed of the impinging flow.

The regime of a stratified airflow over an isolated mountain is characterized by the local Froude number Fr_m,which is defined by (U/Nh_m), where U is the wind speed, h_m is the height of the mountain, and N is the buoyancy frequency. When $Fr_m \gg 1$, the flow passes over the obstacle creating mountain waves, with small lateral displacements at the lowest levels. When its value

TABLE 1. Orographic parameters of the studied obstacles.

Variable	Mountain range of North Basse-Terre	Soufrière
h_m (m)	500	1460
L_m (km)	11	12
l_m (km)	6	10
B	1.83	1.09
N (s^{-1})	10^{-2}	10^{-2}
WTW $U = 3\,m\,s^{-1}$		
Fr_m	0.60	0.21
$\hat{h}$	1.67	4.76
MTW $U = 6\,m\,s^{-1}$		
Fr_m	1.20	0.41
$\hat{h}$	0.83	2.44
STW $U = 12\,m\,s^{-1}$		
Fr_m	2.40	0.82
$\hat{h}$	0.42	1.22

is well below unity, the flow can be blocked on the windward side of the mountain and must split around the obstacle. In this study, two other free parameters introduced by Smith (1989), are used: the nondimensional mountain height ($\hat{h} = Nh_m/U = 1/Fr_m$) and the mountain aspect ratio $\beta(L_m/l_m)$, where L_m is the half-width of the mountain and l_m is the half-length of the mountain. The nonrotational flow can shift from a "flow over" to a "flow around" regime when the nondimensional mountain height increases above a critical value, such as 1.2 for an axisymetric Gaussian mountain (Smith and Grønås 1993; Smolarkiewicz and Rotuno 1989). Bauer et al. (2000) showed that the change of the flow regime is a function of β: the larger β, the smaller the nondimensional mountain value of blocking.

In this article, the behavior of the flow impinging two types of obstacles in the Guadeloupe archipelago is analyzed: axisymmetric mountain ($\beta = 1$) and wide mountain ($\beta > 1$), respectively, La Soufrière and the mountain range of North Basse-Terre.

Geophysical-scale parameters (Table 1) are computed with previous formula for the three studied weather types: WTW, MTW, and STW. Each weather type is characterized by a mean daytime wind speed.

The numerical study of Bauer et al. (2000) was done for obstacles with β range values of [0.25, 4] and $\hat{h}$ range values of [0.25, 5]. He summed up the results in several diagrams where he represented airflow perturbations as a function of the variables $(\beta, \hat{h})$. These results are used to determine coarsely orographic effects of Guadeloupe on adiabatic flows. Heat transfers are not taken into account.

The mountain range of North Basse-Terre represents a barrier obstacle with its horizontal aspect ratio value of 1.83. The STW ($Fr_m = 2.4$) would produce weakly nonlinear patterns associated with a maximum relative velocity reduction of 25% on the windward side and 5% on the leeward side. During MTW ($Fr_m = 1.2$), on the lee side, the wave breaking would induce a maximum relative velocity surplus of 73%. The velocity reduction could reach 65% on the windward side and 37% on the leeward side. At low levels, weak trade winds ($Fr_m = 0.6$) must flow around the mountain range of North Basse-Terre or reverse. In this case, the maximum relative velocity deceleration could reach 125% on the windward side and 185% on the leeward side (linked with the presence of lee vortices). On both sides of the obstacle, there would be reversed flows.

The volcano of La Soufrière is the tallest obstacle for the airflow ($h_m = 1460$ m) with its shape of Gaussian axisymmetric mountain ($\beta = 1$). Based on Bauer et al. (2000), numerical results were too perturbed to examine the range in detail (about $\hat{h} \geq 2$). Thus, his diagram indicates the maximum values of velocity reduction on the slopes of this mountain only for STW ($\hat{h} = 1.22$). In this case ($Fr_m = 0.82$), the velocity deceleration could reach 80% on the windward side and 135% on the leeward side, the velocity surplus on the lee side could peak at 54%. Under this weather type, the volcano of la Soufrière would generate a wave breaking and lee vortices without windward blocking. Typical weather of MTW ($Fr_m = 0.41$) would produce wave breaking, lee vortex formation, and windward stagnation inducing an upslope reversed flow. The same effects would be observed during WTW ($Fr_m = 0.21$), except for the wave breaking. As said by Bauer et al. (2000), this absence of wave breaking would be caused by a weak vertical transport of the wave energy.

According to these preliminary results, Basse-Terre Island with its complex topography would produce different local wind circulations depending on trade wind strength. That includes the reversal of wind direction. To study these orographic-induced wind circulations in this island of Guadeloupe, it is necessary to use a local scale model. The real-case simulations with WRF showed the impact of thermal effects on these endogenous orographic circulations. Grande-Terre Island has a relatively flat topography. In this area, local circulations would be essentially driven by spatiotemporal variations of the surface temperature. In the following parts of the study, WTW, MTW, and STW weather types will be characterized by the respective Froude number values of 0.21, 0.41, and 0.82, respectively.

c. *Diurnal variability*

Over the islands of the Guadeloupe archipelago, the 2-m temperature usually increases by 5°C between 0600 and 1000 LT and reaches its maximum value at 1300 LT (Brévignon 2003). The radiative cooling starts at the end

of the afternoon (1700 LT) and the minimum temperature is reached the following morning at 0500 LT.

During his Ph.D. study, D'Alexis (2011) examined the relationship between the 2-m temperature and 10-m wind speed diurnal cycles that were averaged for 6 months during the 2008 dry season. DES is characterized by sustained winds (7–8 $m\,s^{-1}$) with an absence of diurnal variations in intensity. Wind data from this station may be used to describe coarsely the impinging synoptic wind. For RZT and ARN, which are under the influence of the inland regime, hourly temperatures and wind speeds seem to have a quasi-synchronous evolution.

Temperature diurnal cycles and the yearly averaged temperature of air over sea (27° ± 0.5°C) indicate that the greatest thermal contrast between land and sea occurs during the night (sea–RZT contrast peak of 4.7°C at 0500 LT). Moreover, wind speed diurnal cycles show that major differences between synoptic wind (DES) and local wind at inland stations appear from radiative cooling starting time. This may suggest that at nighttime, local circulations would be better marked than in the daytime. In the case of RZT, from midnight on there is usually an almost total absence of wind. Because of nocturnal cooling, a cold surface layer grows over Grande-Terre Island, and warmer trade winds must flow above this layer (Brévignon 2003).

During the night, in some cases of weak to moderate trade winds, light land breezes on the windward coast of Grande-Terre (Bleuse and Bleuse 1997) and reversed lower-levels flows on the windward coast of Basse-Terre Island (D'Alexis et al. 2011) have been observed. Both these local nocturnal winds, blowing with a westerly direction and speed lower than 2 $m\,s^{-1}$, seem to push offshore lower-levels trade winds.

To illustrate the second nocturnal westerly flow, WTW diurnal cycle (4–5 December 2007) is studied at ARN. A sudden fall in temperature (−1.10°C), in wind speed (−1.45 $m\,s^{-1}$), associated with a reverse in wind direction (southeast to west), is observed in less than 10 min at 2000 LT. From this moment to the next morning, the wind keeps speed values below 1.5 $m\,s^{-1}$ and a west-northwest direction. These observational data indicate a sudden transition from weak synoptic winds to a cold westerly flow in this area. At 2000 LT, the thermal contrast between the air over sea and ARN is lower than 2°C. Thus, this gravity current would probably be mainly induced by the orography and the slope thermal contrasts (drainage of accumulated cold air mass at the crest of the Basse-Terre mountain range).

In the present work, diurnal cycles of the previously selected days of WTW, MTW, and STW have been studied with observational data from ARN, DES, RZT, and the National Data Buoy Center 42059 buoy located in the eastern Caribbean (15.058°N, 67.528°W). The month of December is characterized by the weakest solar radiation in the year. During the three weather types, the mean sea surface temperature registered by the buoy is 27.6°C with slight diurnal variations of 0.2°C. Thus, the land–sea thermal contrast will be mainly driven by the island. The observational data show that land diurnal thermal amplitude decreases when the trade winds become stronger. Strong winds would mask the thermal diurnal cycle, by enhancing air mixing in the lower layers and by the advection of MBL conditions on land. Under any type of weather, the station of RZT presents the greatest values of 2-m thermal amplitude (respectively, 9.4°, 9.2°, and 6.2°C for WTW, MTW, and STW, respectively). These high values must be linked with the weak albedo of the RZT urban area. Minimum wind speed values lower than 1 $m\,s^{-1}$ at nighttime, indicate that RZT and ARN are under the strong influence of the nocturnal cold stable layer. During these nights, local flows orographically or thermally induced (previously described) can be developed in this inland regime area (middle of the archipelago, Fig. 1). The complex topography of the archipelago and its nocturnal land–sea air thermal contrast, suggest that these cases of particular nocturnal circulations cannot be isolated.

3. Model description and evaluation

a. Model description

The atmospheric model employed for the real-case simulations is WRF (Skamarock et al. 2008). To study the local circulations induced by interactions between synoptic winds and small islands such as the Guadeloupe archipelago, a two-way four-level downscaling (grid spacing in km: 27, 9, 3, and 1) is used (Fig. 3). The outermost domain (domain 1) covers 80 × 80 grid cells in the central Atlantic area from South America to the Dominican Republic. Domain 2 covers 121 × 109 grid cells in the Lesser Antilles. Domain 3 covers 112 × 91 grid cells in the area from Dominica Island to St. Kitts and Nevis Islands. The innermost domain (domain 4) covers 130 × 112 grid cells on the Guadeloupe archipelago. In the WRF Preprocessing System, terrestrial data are provided by the U.S. Geological Survey (USGS). However, the topography of the innermost domain was interpolated from the Institut Géographique National (IGN) 50-m topographic map of the Guadeloupe archipelago. The smoothing of high peaks and valleys is illustrated by the elevation comparison between the 50-m IGN and 1-km WRF maps (Fig. 1). The vertical model grid contains 72 unequally spaced eta levels with the lowest level at 13 m AGL. However, the model provides

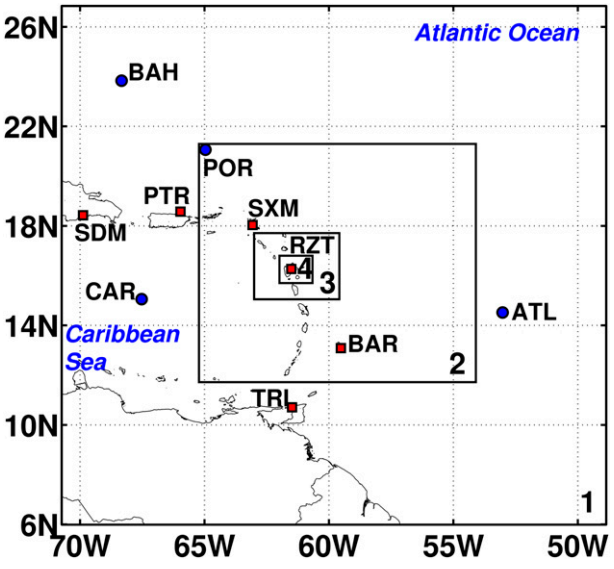

FIG. 3. Description of the four domains employed in the WRF numerical simulation, with respective resolutions of 27, 9, 3, and 1 km, soundings (TRI, BAR, RZT, SXM, PTR, and SDM: red squares) and NDBC buoys (ATL, CAR, POR, and BAH: blue circles).

typical surface variables. The 2-m temperature is diagnosed from the model-level fields and the skin level. The 10-m wind based on Monin–Obukhov similarity theory, is computed. The model top is set at the troposphere layer top (i.e., 50 hPa). This study deals with orographic (maximum MSL elevation of 1460 m) and thermal impacts on island-scale circulations. Thus, the lower layers of the troposphere (3000 first meters) are set with 43 vertical levels. Physics parameterizations are close to the ones found in numerical studies on tropical islands (Jury et al. 2009; Lefèvre et al. 2010). The nonlocal-*K* PBL Yonsei University scheme (Hong et al. 2006) with the Monin–Obukhov surface layer parameterization is chosen. Microphysics are parameterized by the WRF single-moment 6-class microphysics scheme (Hong and Lim 2006), which is suitable for high-resolution simulations contrary to the WRF single-moment 3-class microphysics scheme used by Lefèvre et al. (2010). For radiation parameterization, the Rapid Radiative Transfer Model (RRTM) longwave scheme (Mlawer et al. 1997) and the Dudhia shortwave scheme (Dudhia 1989) are selected. Lesser Antilles volcanic islands, like Martinique, Dominica, and Guadeloupe have a very complex topography. To well simulate radiative forcing, slope effects and neighboring-point shadow effects are added for domains 3 and 4. The Noah land surface model (Chen and Dudhia 2001), which includes soil temperature and moisture in four layers is selected. In domain 1, the Kain–Fritsch scheme (Kain 2004) is added to parameterize the convection. In the other domains, the model explicitly resolves the convections. The SST skin option is activated in order to simulate the sea skin temperature diurnal cycle. The model is 6-hourly initialized with meteorological data from the 1° National Centers for Environmental Prediction (NCEP) Final Analysis (FNL) operational model global tropospheric analyses (continuing from July 1999, available online at http://dss.ucar.edu/datasets/ds083.2/). This includes skin temperature fields. Model output data are hourly available for the four domains.

WRF has the present configuration for three simulations of 60 h: the WTW case (from 1800 UTC 2 December to 0600 UTC 5 December 2007), the STW case (from 1800 UTC 13 December to 0600 UTC 16 December 2007), and the MTW case (from 1800 UTC 23 December to 0600 UTC 26 December 2007). In all cases, the first 12-h results are not taken into account for the analysis. This is the typical spinup time period (Hu et al. 2010).

b. *Model evaluation*

1) EVALUATION OF SURFACE DATA

The error estimators (MBE, RMSE, MAE, IOA, and IOA2) are described in the appendix. The RMSE and the IOA are mostly used in the literature to summarize mean differences between the forecast and the observational data. However, according to Willmott and Matsuura (2005), because of the sum of squared errors characterizing these parameters, large errors have a relatively greater influence on the total square error than smaller ones (unlike the MAE). The present short time simulations: with very few comparison locations (low number of reliable weather stations), would be more affected by this problem. To fix it, the MAE and the IOA2 are chosen instead of the RMSE and the IOA, on the recommendation of Willmott and Matsuura (2005) and Willmott et al. (2012). The following IOA2 values: negative, between 0 and 0.5 and above 0.5, are considered as bad, good, and very good, respectively.

The observational land surface data are extracted from the five weather stations available in domain 4: RZT, DES, MOU, GBD, and ARN (Fig. 1). The hourly data studied are: 10-min means, 2-m air temperature, and 10-m wind speed and direction. RZT, DES, MOU, and GBD have an accuracy of 0.1°C for temperature, 1 m s^{-1} for wind speed, and 10° for wind direction. ARN has an accuracy of 0.2°C for temperature, 2% (with a resolution of 0.01 m s^{-1}) for wind speed, and 3° for wind direction.

The observational sea surface data are extracted from four National Data Buoy Center buoys: POR (ID 41043, 21.061°N, 64.966°W) located in domain 2, BAH (ID 41046,

TABLE 2. Surface data evaluation.

	ARN	RZT	DES	MOU	GBD	ATL	CAR	BAH	POR
Air temperature (°C)									
No. of data points	144	144	144	144	144	144	144	144	144
Obs mean	24.8	25.1	26.7	25.2	26.0	26.2	27.1	24.7	25.8
Obs std dev	2.5	2.8	1.3	2.6	1.9	0.5	0.5	0.4	0.4
MBE	−0.3	−0.8	−1.1	−0.1	−1.3	−0.3	−0.6	−0.3	−0.6
MAE	1.0	1.2	1.2	1.5	1.4	0.4	0.7	0.4	0.5
IOA2	0.7	0.7	0.5	0.5	0.6	0.5	0.4	0.4	0.5
Sea surface temperature (°C)									
No. of data points	—	—	—	—	—	144	144	144	144
Obs mean	—	—	—	—	—	27.0	27.6	25.6	26.8
Obs std dev	—	—	—	—	—	0.3	0.2	0.2	0.3
MBE	—	—	—	—	—	0.0	0.1	0.2	−0.1
MAE	—	—	—	—	—	0.2	0.1	0.2	0.2
IOA2	—	—	—	—	—	0.7	0.7	0.6	0.8
Wind speed ($m\,s^{-1}$)									
No. of data points	144	144	144	144	144	144	144	144	144
Obs mean	3.5	3.0	7.5	3.1	5.1	6.3	7.9	5.9	7.5
Obs std dev	2.3	2.2	3.7	1.9	2.8	2.8	2.0	2.2	2.1
MBE	−0.1	0.2	−1.8	1.7	−0.3	1.7	1.0	1.5	0.4
MAE	1.3	1.1	2.1	2.0	1.1	1.8	1.2	1.6	1.9
IOA2	0.7	0.7	0.7	0.6	0.7	0.5	0.6	0.7	0.7
Wind direction (°N)									
No. of data points	144	120	144	135	143	144	144	144	144
Obs mean	166.8	90.3	104.9	97.4	87.8	77.6	69.8	115.4	82.0
Obs std dev	83.3	50.1	19.6	78.2	54.3	35.4	18.0	61.5	15.8
MBE	−48.6	4.7	−19.2	−1.2	−10.1	−1.9	−0.7	−8.7	−15.9
MAE	54.2	31.0	33.4	58.4	29.7	16.6	11.3	16.9	18.6
IOA2	0.7	0.4	0.6	0.2	0.4	0.6	0.6	0.8	0.4

23.838°N, 68.333°W), CAR (ID 42059, 15.058°N, 67.528°W), and ATL (ID 41040, 14.516°N, 53.024°W), which are located in domain 1 (Fig. 3). The hourly data studied are 10-min means, sea surface temperature, 4-m air temperature, and 5-m wind speed and direction. The four buoys have an accuracy of 1°C for sea surface temperature, 1°C for air temperature, $1\,m\,s^{-1}$ for wind speed, and 10° for wind direction. WRF output variables are extracted at the closest grid points of each station. Model-prediction error estimators are computed on the three simulations of 48 h ($n = 144$) and reported on in Table 2. For wind speeds lower than $1\,m\,s^{-1}$, RZT, DES, MOU, and GBD do not record wind direction values, this is why there are missing data in wind directions statistics. Concerning buoys, sea surface temperature, 4-m air temperature, and 5-m wind speed and direction are compared with skin temperature, 2-m air temperature, and 10-m wind speed and direction from the model, respectively. In the table, all values of IOA2 are positive: it means that at any station, the model gives good prediction for air temperature, sea surface temperature, wind speed, and wind direction. Generally, the model presents better scores at land stations. This would be due to vertical approximation of buoys data. However the sea surface temperature is very well simulated with all IOA2 values above 0.5. Over land, wind speed is the best simulated variable with very good values of IOA2. For this variable, the worst prediction appears at MOU (IOA2 = 0.6 and MAE = $2.0\,m\,s^{-1}$), which is at the limit between the inland and windward regimes. The wind direction statistics show an important variability of this parameter during the three simulations, this is the worst simulated variable over land. But globally the model has good prediction of this variable with the best score occurring at ARN. Concerning the 2-m temperature, generally the model has good performance with a tendency to underestimation over land and sea. This is the worst simulated variable over sea. Inland stations (ARN, RZT, and GBD) have very good scores whereas windward coastal stations (MOU and DES) have just good scores. This could suggest that WRF simulates a better thermal diurnal cycle undisturbed by the marine ABL conditions. For all variables and all simulations, MOU presents the worst score of IOA2: this could confirm its hybrid location (between inland and windward regimes).

2) EVALUATION OF UPPER-AIR DATA

The first problem encountered to evaluate the simulation of atmospheric lower layers conditions is the lack of radiosounding data in domain 4, during short time

TABLE 3. Upper-air data evaluation with 35 soundings.

	Pressure levels (hPa)															
	1000	950	925	900	850	800	700	650	600	500	400	300	250	200	150	100
No. of data points	35	35	35	35	35	35	35	35	35	35	35	35	35	35	35	35
Dry potential temperature (K)																
Obs mean	297.0	298.9	299.5	300.2	302.4	305.2	311.6	315.0	318.4	324.8	331.1	338.2	342.2	347.8	355.5	379.6
Obs std dev	1.1	1.0	1.0	1.3	1.2	1.4	1.5	1.9	1.8	2.0	2.3	2.7	2.0	2.7	4.2	3.2
MBE	0.2	−0.9	−1.0	−0.8	0.1	0.2	0.5	0.9	0.3	0.2	0.2	−0.1	−0.1	−0.7	−1.0	−2.1
MAE	0.8	1.0	1.1	1.1	0.9	0.8	1.0	1.3	1.2	1.0	0.8	0.9	0.9	1.3	1.5	3.0
IOA2	0.5	0.4	0.5	0.5	0.6	0.7	0.7	0.5	0.4	0.6	0.8	0.8	0.7	0.6	0.8	0.5
Water vapor mixing ratio ($g\,kg^{-1}$)																
Obs mean	15.4	13.8	12.9	11.7	9.8	7.5	3.1	2.1	1.1	0.7	0.5	0.2	—	—	—	—
Obs std dev	1.4	1.5	1.3	1.4	2.2	3.4	2.2	1.9	1.6	0.9	0.7	0.1	—	—	—	—
MBE	−0.1	0.4	0.4	0.0	−1.4	−1.4	−0.3	−0.4	0.2	−0.1	−0.1	0.2	—	—	—	—
MAE	1.0	1.3	1.1	1.5	2.7	2.9	2.0	1.4	1.0	0.4	0.3	0.1	—	—	—	—
IOA2	0.4	0.2	0.3	0.4	0.4	0.3	0.5	0.5	0.5	0.7	0.6	0.5	—	—	—	—
Wind speed ($m\,s^{-1}$)																
Obs mean	4.8	8.5	8.9	8.8	8.5	8.1	8.2	8.2	9.1	10.0	7.8	11.8	17.2	21.0	20.8	12.9
Obs std dev	2.7	4.3	4.4	4.2	3.9	4.1	4.8	4.3	3.8	4.0	3.7	5.4	7.5	9.5	8.4	3.5
MBE	2.8	1.1	0.9	1.0	0.7	0.4	0.0	−0.1	−0.5	−0.6	0.8	0.2	−0.2	0.2	1.1	0.5
MAE	3.2	2.2	1.9	1.9	2.5	2.4	2.4	2.0	2.4	2.5	2.0	2.4	3.3	2.6	3.6	2.4
IOA2	0.6	0.7	0.7	0.8	0.7	0.7	0.7	0.7	0.6	0.6	0.7	0.7	0.7	0.9	0.8	0.6
Wind direction (°N)																
Obs mean	67.3	71.3	73.1	74.2	73.4	78.1	111.7	120.9	119.7	124.7	152.3	252.9	237.1	215.9	204.4	176.1
Obs std dev	80.1	26.7	17.7	17.7	22.1	26.8	73.2	73.6	72.3	99.8	121.6	97.4	103.0	107.1	120.9	127.6
MBE	−1.2	−2.0	−2.5	−0.6	7.2	11.1	−19.1	−4.6	4.7	−4.5	1.2	1.6	15.4	24.9	10.6	27.8
MAE	45.5	15.0	12.1	12.9	22.8	28.1	37.1	34.2	19.6	22.9	62.7	33.3	25.3	31.5	25.0	48.6
IOA2	−0.1	0.5	0.5	0.6	0.4	0.4	0.6	0.7	0.8	0.8	0.7	0.8	0.8	0.8	0.9	0.8

simulations like ours. During the dry season, one daily 1200 UTC sounding is launched from RZT. Thus, for the three 48-h time simulation, there are only six observed profiles. To get more comparison points, other 1200 UTC soundings were used: BAR (ID 78954, Barbados) and SXM (ID 78866, St. Martin) are located in domain 2, TRI (ID 78970, Trinidad), PTR (ID 78526, Puerto Rico), and SDM (ID 78486, Dominican Republic) are located in domain 1 (Fig. 3). Moreover, the soundings include approximately half the number of WRF vertical levels. To compute statistical tools used previously, radiosoundings and model vertical profiles data are interpolated (with cubic spline method) at the same pressure levels. The model ingests these observational profiles through NCEP FNL analyses at 1200 UTC. To estimate the ability of WRF to predict the stratification, the 1100 UTC WRF vertical profiles are evaluated.

Results of the 35 comparisons (TRI has a missing sounding) at each level between interpolated profiles from radiosoundings and model are reported for four variables (Table 3): dry potential temperature, water vapor mixing ratio, wind speed, and direction. Water vapor mixing ratio errors cannot be computed above 300 hPa because of missing measures. Overall the model predicts well the troposphere stratification, except the wind direction at 1000 hPa (IOA2 = −0.1). This is probably induced by turbulence motions generated by the transition period between nocturnal and diurnal conditions. The wind direction starts to be very well simulated from the 650-hPa level. The best simulated variable is the wind speed with very good values of IOA2 for all pressure levels. Mean bias errors indicate that the model tends to overestimate wind speeds up to the 700-hPa level. The WRF dry potential temperature presents good to very good scores of prediction. The water vapor mixing ratio has good values of IOA2, mainly lower than 0.6.

4. The 1-km numerical results over Guadeloupe (domain 4)

The study of the main factors forcing the local airflow circulations over the archipelago indicates that the larger the Froude number, the smaller the orographic and thermal effects. Thus, numerical results will be analyzed in the following order: STW ($Fr_m = 0.82$), MTW ($Fr_m = 0.41$), and WTW ($Fr_m = 0.21$).

a. Surface energy budget

Thermal airflow circulations are driven by the spatiotemporal evolution of surface energy budget, defined without snow processes in the Noah land surface model

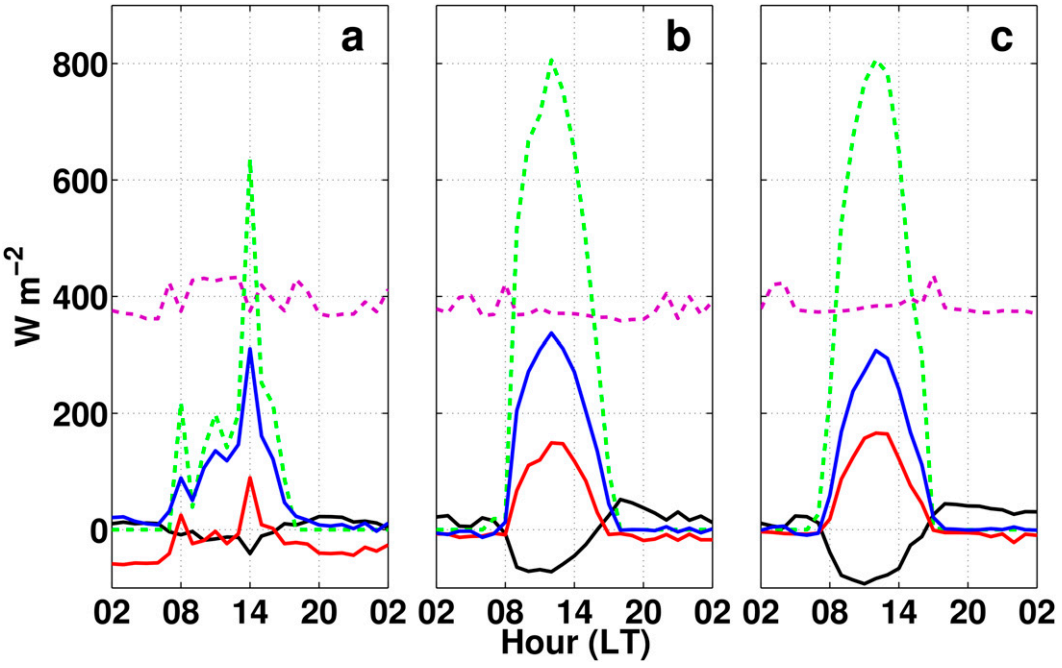

FIG. 4. WRF diurnal surface energy budget at ARN location for each weather type: (a) STW 14 Dec 2007 (Fr_m = 0.82), (b) MTW 24 Dec 2007 (Fr_m = 0.41), and (c) WTW 3 Dec 2007 (Fr_m = 0.21), with five fluxes (W m^{-2}), the downward shortwave radiation SD (green dashed line), the downward longwave LD (magenta dashed line), the latent heat flux LH (blue solid line), the sensible heat flux SH (red solid line), and the ground heat flux G (black solid line).

(Chen and Dudhia 2001) as $(1-\alpha)\text{SD} + \text{LD} - \varepsilon\sigma T_s^4 = \text{SH} + \text{LH} + G$, where α is the albedo (dimensionless); SD and LD are the downward shortwave and longwave radiation (W m^{-2}), respectively; ε is the emissivity (dimensionless);σ is the Boltzmann constant (W m^{-2} K^{-4}); T_s is the skin temperature (K); and SH, LH, and G are the sensible, latent, and ground heat flux (W m^{-2}), respectively. For the three weather types, the simulated diurnal surface energy balance is examined at ARN where particular airflow circulations were measured. Under the three weather types, the Bowen ratio (i.e., β_o = SH/LH) is less than one during the day, thus a great proportion of exchanged energy passes to the atmosphere as latent heat (Fig. 4). It is the opposite at nighttime. The Bowen ratio seems to decrease as the strength of the trade wind increases. The minimum β_o of 0.28 occurs during STW. Under this weather type the maximum downward shortwave radiation is very low (−172 W m^{-2}) and occurs at 1400 LT instead of typical MTW and WTW maximum time of 1200 LT. This would be induced by the cloud cover. In this case the elevation of the skin temperature will be inhibited.

In the following parts of the study, the sensible heat flux effects on the thermally driven flow are analyzed. Unlike the latent heat flux, the sensible heat flux directly induces changes in near-surface air temperature: $\text{SH} = \rho C_p C_h |V|(T_s - T_1)$, where ρ is the air density (kg m^{-3}); C_p is the air heat capacity (J m^{-3} K^{-1}); C_h is the surface exchange coefficient for heat and moisture, depending on surface roughness lengths (dimensionless); V is the surface layer wind speed (m s^{-1}); and T_s and T_1 are the skin and the near-surface air temperature (K), respectively. SH could increase dynamically with the surface layer wind speed. The latent heat flux, largely provided in Guadeloupe by strong convective rainfall and soil moisture will be studied in future works.

b. *Case of STW (Fr_m = 0.82)*

At daytime, 1400 LT 14 December 2007, the impinging flow is almost uniform with a wind speed of 12 m s^{-1} and an east-northeast direction (Fig. 5a1). In the study, low clouds are defined between the surface and the 850-hPa level. There is a particular clear sky over low land areas; the strong trade winds inhibit the convection over low land areas (Fig. 5a2). An orographically induced compact low cloud cover, decreases the skin temperature below 24°C on the mountains of Basse-Terre (Fig. 5a3). This results in the major diurnal negative value of SH (−50 W m^{-2}). The extreme values of SH and T_s, which are 350 W m^{-2} and 34°C, respectively, correspond to urban land-use areas. The airflow seems to have a weakly nonlinear pattern over the mountainous range of north Basse-Terre: the air mass flows above the obstacle with small lateral deflections, an acceleration at the crest

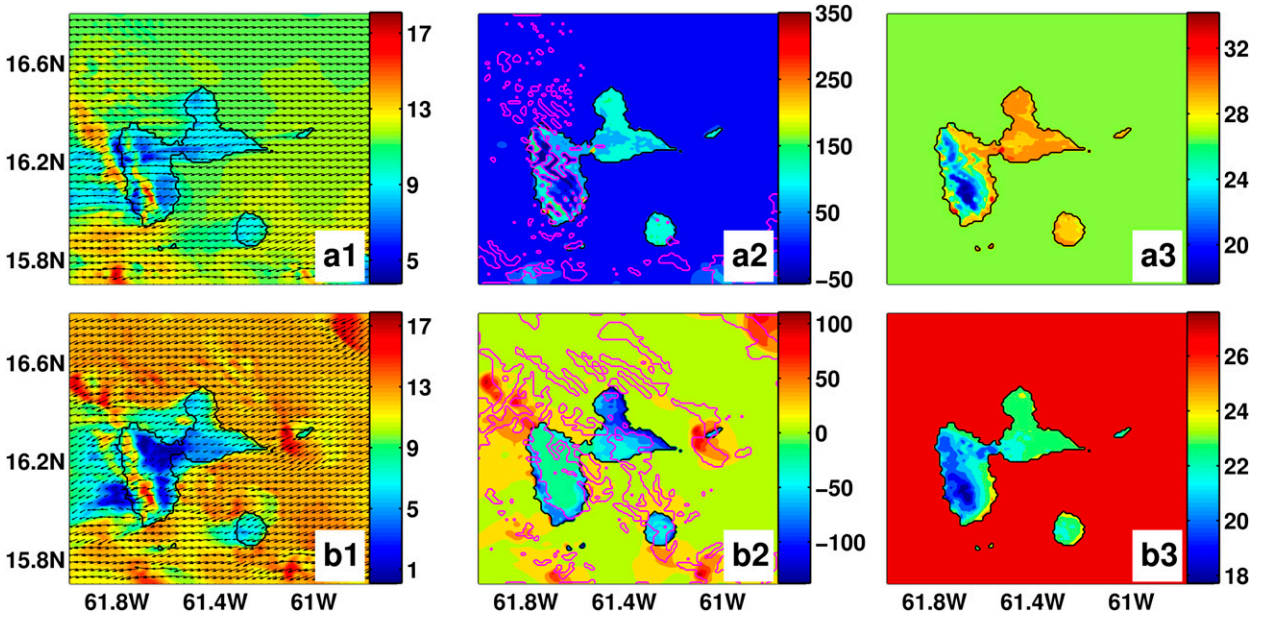

FIG. 5. STW (Fr_m = 0.82) local circulations at (a1)–(a3) daytime 1400 LT 14 Dec 2007 and (b1)–(b3) nighttime 0400 LT 15 Dec 2007: (a1),(b1) 10-m winds (speed in m s^{-1}); (a2),(b2) sensible heat flux (SH in W m^{-2}) and low clouds (below 850-hPa level) (magenta contours); and (a3),(b3) skin temperature (T_s in °C).

and a deceleration on the leeward coast. In this area near the Caribbean Sea, a flow acceleration band parallel to the mountainous range, followed by a deceleration, would suggest a propagation of lee waves. At La Soufrière the air mass flows above and around the volcano, and a thin wave breaking, associated with a weak wake, occurs.

At nighttime, 0400 LT 15 December 2007, nocturnal trade winds keep the speed of 12 m s^{-1} and the east-northeast direction, but the wind field is less uniform, including more Atlantic disturbances (Fig. 5b1). The important cloud cover, advected from the sea on the low land areas and orographically induced on the mountains of Basse-Terre, inhibits the radiative cooling (Figs. 5b2 and 5b3). Over the low land areas, the thermal sea–land contrast has a low value of 4°C. In high lands T_s is poorly cold (17.8°C). Like in the diurnal case, this weather type presents a large nocturnal negative value of SH, dynamically forced by the surface layer wind speed on the windward coasts of the archipelago. The air mass slowed by the cold land surface is more impacted by the orography. In the north part, the diurnal weakly nonlinear regime changes to wave breaking regime. At La Soufrière, the wave breaking and the wake are better defined.

c. *Case of MTW* (Fr_m = 0.41)

At daytime, 1400 LT 24 December 2007, the Atlantic wind field has globally a speed of 6 m s^{-1} and a uniform east direction (Fig. 6a1). Because of the land–sea thermal contrast (mean value of 4°C), marine airflows tend to converge over land (Fig. 6a3). This generates a line of low convective clouds over Grande-Terre (Fig. 6a2). Other convective clouds are generated on the mountainous island of Basse-Terre. As the downward shortwave radiation decreases at cloud locations, the heating of the soil is inhibited. In some cases, the soil is cooler than the near-surface air, thus the sensible heat flux (SH) may be negative. The moderate wind speed allows the impinging air mass to flow above and around the volcano of La Soufrière. A wave breaking generates a wind acceleration area on the lee slopes and a calm wind area on the leeward coast. This results in a wake linked with a sea-breeze circulation. At this location characterized by a clear sky, the land–sea thermal contrast reaches 6°C. The onshore development on upslopes would be inhibited by the strong plunging flows due to the wave breaking.

At nighttime, 0400 LT 25 December 2007, the impinging flow has a speed of 7 m s^{-1} and an east-northeast direction (Fig. 6b1). Over low lands, the sea–land thermal contrast is 4°C greater than the STW one at the same hour (Fig. 6b3). However the trade wind intensity inhibits the development of land-breeze circulations. In Grande-Terre the weak airflow diverges without reversal in direction and without offshore extension. Over the high lands of Basse-Terre, the impinging airflow is blocked on the windward side of the volcano. A katabatic flow occurs linked with a minimum T_s 4°C lower than the STW one at the same location (i.e., at the top of

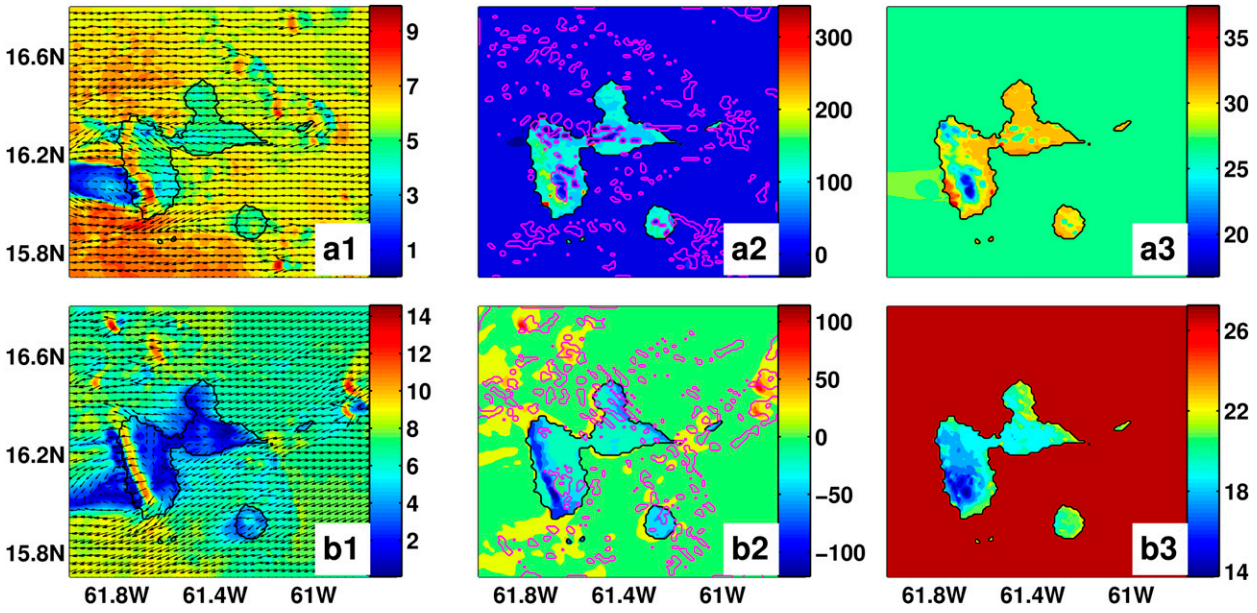

FIG. 6. MTW ($Fr_m = 0.41$) local circulations at (a1)–(a3) daytime 1400 LT 24 Dec 2007 and (b1)–(b3) nighttime 0400 LT 25 Dec 2007: (a1),(b1) 10-m winds (speed in $m\,s^{-1}$); (a2),(b2) sensible heat flux (SH in $W\,m^{-2}$) and low clouds (below 850-hPa level) (magenta contours); and (a3),(b3) skin temperature (T_s in °C).

the volcano). This reversed circulation seems weak with no extension to the sea. On the lee side, a strong wave breaking occurs associated with maximum absolute values of SH, dynamically forced by the surface layer wind speed (Fig. 6b2). The diurnal wake is still present with a northeast direction.

d. Case of WTW ($Fr_m = 0.21$)

At daytime, 1400 LT 3 December 2007, the trade winds a have wind speed lower than $3\,m\,s^{-1}$ with a direction between the northeast and east (Fig. 7a1). Because of the position of the low pressure center in the

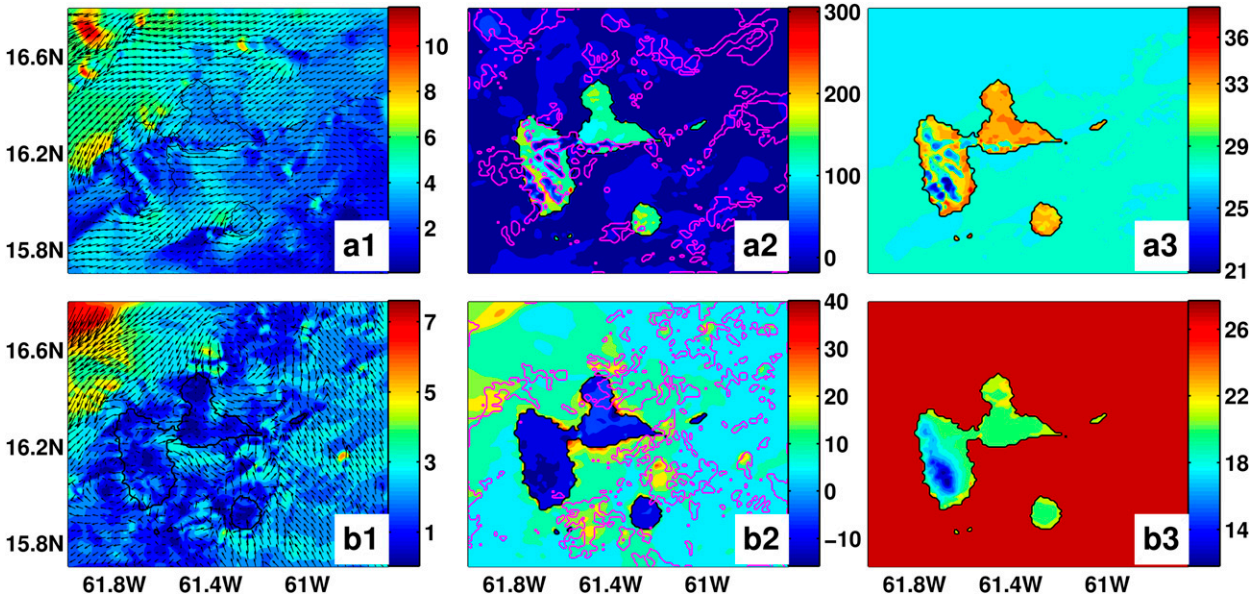

FIG. 7. WTW ($Fr_m = 0.21$) local circulations at (a1)–(a3) daytime 1400 LT 3 Dec 2007 and (b1)–(b3) nighttime 0400 LT 4 Dec 2007: (a1),(b1) 10-m winds (speed in $m\,s^{-1}$); (a2),(b2) sensible heat flux (SH in $W\,m^{-2}$) and low clouds (below 850-hPa level) (magenta contours); and (a3),(b3) skin temperature (T_s in °C).

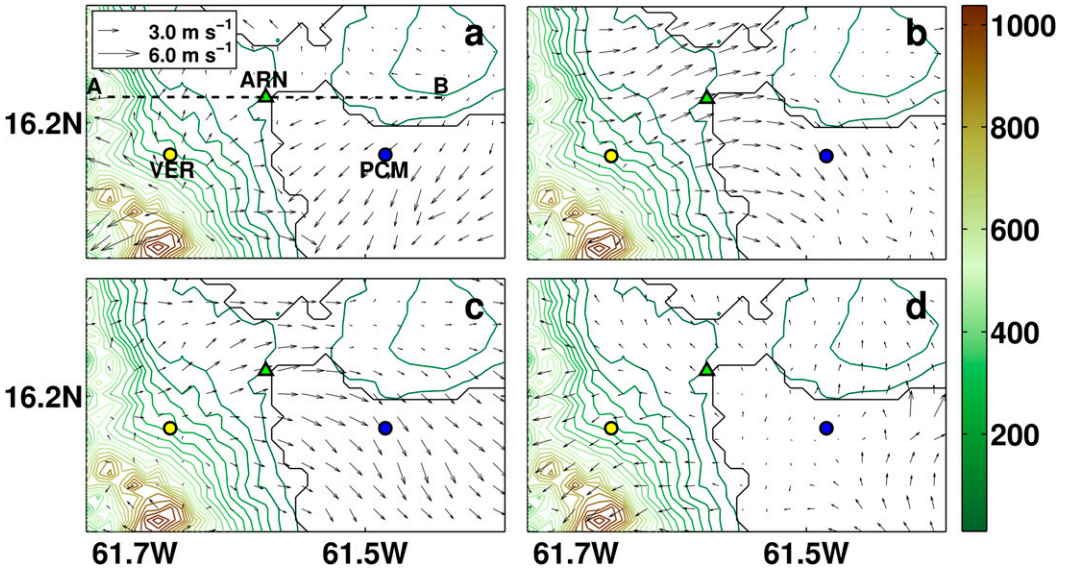

FIG. 8. Evolution of the westerly nocturnal downslope flow during the night of 3–4 Dec 2007 (WTW, $Fr_m = 0.21$) in the region of interest at (a) 2000, (b) 0200, (c) 0400, and (d) 0900 LT: the 10-m wind arrows ($m\,s^{-1}$), elevation heights (m), cross section A–B, and three points of study (VER, ARN, and PCM).

Atlantic Ocean, wind speeds are greater in the northwest corner of the domain. The land–sea thermal contrast is 2°C greater than the MTW contrast (Fig. 7a3). A cloud line is generated on the south coast of Grande-Terre (Fig. 7a2) and there are more convective clouds on the mountainous island of Basse-Terre. The impinging air mass must flow around the volcano of La Soufrière and a wake is generated on the lee side of Basse-Terre Island.

At nighttime, 0400 LT 4 December 2007, the Atlantic wind field has a global speed of 2.5 $m\,s^{-1}$ and significant variations in wind direction. An anticyclonic cell occurs in the northeast of Grande-Terre Island, probably induced by the confluence of southeast and northeast trade wind flows (Fig. 7b1). Over the sea, downdraft motions of clouds induce locations with diverging accelerated flows (Fig. 7b2). Over land the clear sky, including a null cloud cover over the mountain range, enhances the radiative cooling. At low elevation areas the mean sea–land thermal contrast reaches 7°C and the minimum T_s falls below 12°C on high lands (Fig. 7b3). As a result of this and the weak synoptic wind, land-breeze circulations seem to occur all around the main islands. Westerly reversed flows blow on the windward coasts of Grande-Terre, as observed by Bleuse and Bleuse (1997) during the same type of weather. On the windward side of Basse-Terre Island, a westerly katabatic wind flows down with an acceleration area at ARN and extends to the sea (PCM point of study Fig. 1). This katabatic current, observed by D'Alexis (2011) during this same night, joins the South Grande-Terre land breezes. At this time, this coupled westerly circulation extends to 18 km from the windward coast of Basse-Terre. The maximum values of SH at coastal wind acceleration areas keep these offshore cold circulations until sunrise. The WTW katabatic wind is stronger than that of the MTW. This is probably due to the presence during the MTW case of orographic clouds that inhibit the radiative cooling on the mountain (Fig. 6b2). The MTW minimum T_s is 2°C greater than the WTW minimum.

e. *Nocturnal katabatic flow on the windward coast of Basse-Terre during WTW ($Fr_m = 0.21$)*

In the previous paragraph, the model showed its ability to simulate an observed nocturnal reversed flow on the windward coast of Basse-Terre under WTW during the night of 3–4 December 2007. The katabatic flow is examined in region of interest (16.08221°N, 61.7422°W; 16.30165°N, 61.37868°W) (Fig. 8). At 2000 LT (Fig. 8a), the katabatic flow would be generated by a divergence point located at 16.1221°N, 61.6591°W and 567 m MSL height. The confluence between this particular flow and the trade winds occurs on the coast. From 0200 to 0400 LT (Figs. 8b,c), the katabatic wind, stronger than at the previous time, extends to the sea pushing the trade winds offshore. From the initial starting point to Grande-Terre, the reversed flow turns from the southwest direction to the northwest direction. The latter wind direction may be associated with land-breeze circulations occurring on the south coast of

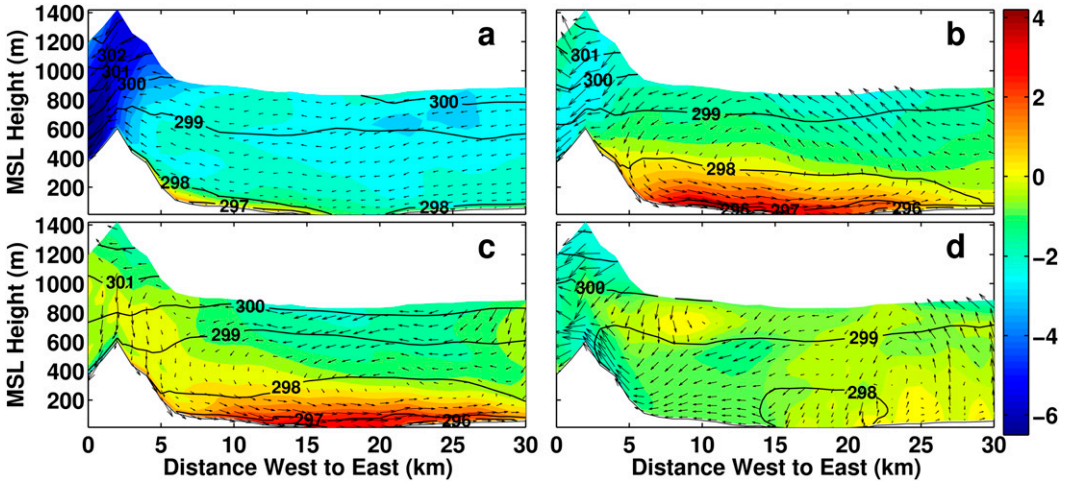

FIG. 9. Evolution of the katabatic flow during the night of 3–4 Dec 2007 (WTW, $Fr_m = 0.21$) along the cross section A–B (Fig. 1b) at (a) 2000, (b) 0200, (c) 0400, and (d) 0900 LT: wind speed arrows (U and $10 \times W$ compounds, m s^{-1}), wind speed color map (U compound, m s^{-1}), and dry potential temperature contours (K) with a step of 1 K.

Grande-Terre. At 1000 LT, the radiative heating of the soil induces anabatic motions that develop on windward slopes of Basse-Terre, while the trade winds reappear in the southeast corner.

The spatiotemporal evolution of the nocturnal reversed flow analyzed in cross section A–B (Fig. 8), including the location of ARN at 15 km on the x axis (Fig. 9), confirms the previous analysis. The katabatic wind is initialized at 2000 LT on a windward slope point (11 km inland with an MSL height of 380 m) of Basse-Terre (Fig. 9a). The weak downwind seems to be limited by the Basse-Terre 298-K isotherm that has a low AGL height and a coastal boundary. At 0200 LT (Fig. 9b), the katabatic wind extending to the sea surface (i.e., the Petit Cul-de-Sac Marin), is close to Grande-Terre. The lower-level flow is stronger and cooler than at the previous time, with the 296-K isotherm at the surface and a maximum longitudinal wind speed of 4 m s^{-1}. The flow is marked by a return current above AGL heights of 400 m which would correspond with the 298-K isotherm. At 0400 LT (Fig. 9c), the cold air mass moves to Grande-Terre island (approximately at a distance of 27 km from its starting point). This fact may be one of the causes explaining the west wind direction observed on the morning radiosounding of RZT. The transition time between the stable nocturnal and the unstable diurnal ABL is represented as 1000 LT (Fig. 9d). At this time, the windward and leeward slopes of the mountain are already hot enough to generate anabatic motions.

Two virtual points of study have been defined in the region of interest: one upstream located on the windward slopes, VER (16.1920°N, 61.6695°W, 235 m MSL), and the other one downstream located over the sea area of Le Petit Cul-de-Sac Marin, PCM (16.1920°N, 61.5033°W, sea level).

Simulated hourly time series are studied for four variables during the period from 1200 LT 3 December to 1200 LT 4 December 2007, at ARN, VER, and PCM, and observational data from ARN were added (Fig. 10). Globally, ARN simulated and observed data fit well for the four variables; the largest biases occur for the wind speed of the katabatic flow, which is overestimated by the model (Fig. 10). At 1700 LT, the sensible heat flux becomes negative at VER and ARN, inducing at 1800 LT a 2-m temperature drop of 1.5°C at these locations. At the same hour the katabatic flow starts at VER, linked with a fall of wind speed and a south wind direction. At 2000 LT, a simultaneous drop in wind speed (below 1 m s^{-1}) and reversal of wind direction occur at ARN. At 0100 LT, the airflow circulation over sea (PCM) also reverses to the west. Between 0700 and 0800 LT, the sensible heat flux becomes positive and 2-m temperature rises by 3°C over VER and ARN. At 0900 LT, the wind direction is back to the east at the three locations.

To study the probable link between these three locations and the spatiotemporal pattern of the katabatic front, the momentum of circulation was plotted in the lower layers (Fig. 11). At VER, the flow has a maximum intensity at 0000 LT, with two secondary peaks (Fig. 11a). A similar signature of flow intensity occurs at ARN (Fig. 11b), 3 h later, with a deeper front (≈250 m) and a momentum of 3.8 kg m^{-2} s^{-1}. This would indicate that the ARN katabatic flow would come from VER. At PCM (Fig. 11c), the three peaks pattern is not found. The maximum intensity peak appears at 0500 LT. The location of PCM would suggest that the signal at this point

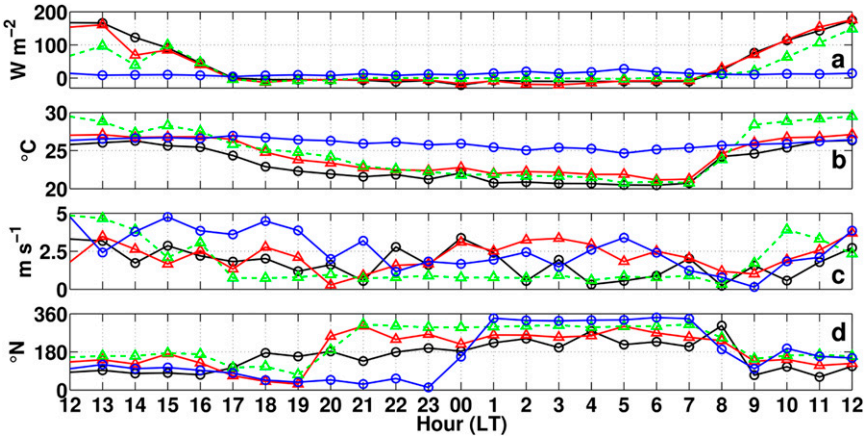

FIG. 10. Comparison between WRF VER (black circles), WRF PCM (blue circles), WRF ARN (red triangles), and observed ARN (green triangles) time series (1200 LT 3 Dec–1200 LT 4 Dec 2007) for four variables: (a) sensible heat flux ($W\,m^{-2}$), (b) 2-m air temperature (°C), (c) 10-m wind speed ($m\,s^{-1}$), and (d) 10-m wind direction (°N).

would be disturbed by the confluence between the Grande-Terre land breeze and the Basse-Terre katabatic flow.

To confirm the previous interpretation, the reverse trajectory of the air mass arriving at the three locations was computed during the period of the katabatic wind. Considering the air mass advected without friction, the motion law for massless particles was resolved. Results show that the katabatic wind starts in the area around the expected point (i.e., 16.1221°N, 61.6591°W, 566 m MSL), previously described (Fig. 8). This wind flows successively to the areas of VER, ARN, and PCM.

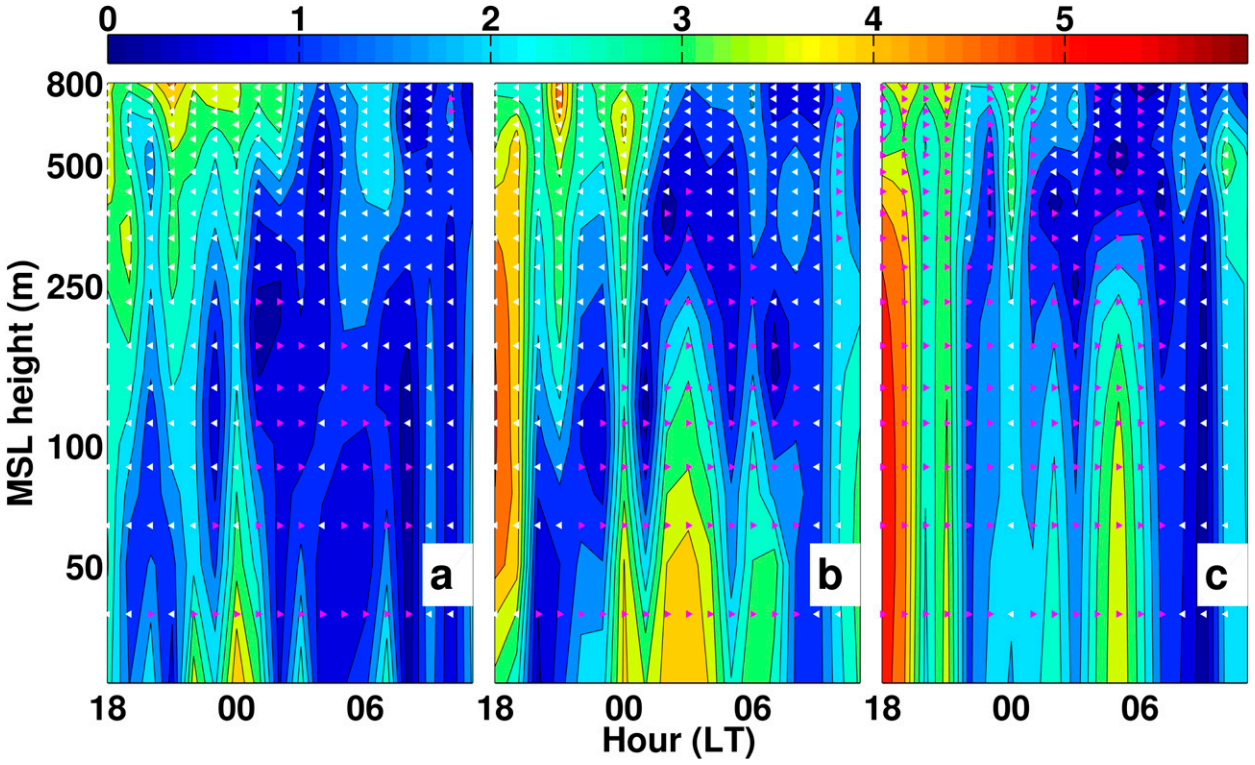

FIG. 11. Temporal log height cross section for the momentum flux ($kg\,m^{-2}\,s^{-1}$) of the katabatic wind during the night of 3–4 Dec 2007 at three points of study: (a) VRN (direction from west to east), (b) ARN (direction from west to east), and (c) PCM (direction from north to south). Triangles represent the direction of the flow function of the propagation direction: (magenta) positive flow and (white) negative flow.

Concerning this last location, two reverse trajectories are possible, one following the katabatic flow and the second following the land-breeze circulation. This supports the different signal of the flow at this location (Fig. 11c).

5. Conclusions

The main goal of this study was to analyze the mechanisms that drive local-scale airflow circulations over the Guadeloupe archipelago, using 1-km WRF. The most important forcings expected in the literature, are the impinging flow velocity, the orography, and the diurnal cycle. Three meteorological situations have been selected during December 2007: STW, MTW, and WTW, which correspond to Froude number values 0.82, 0.41, and 0.21, respectively. For these three weather types and at different locations, simulated typical meteorological variables (the sea surface temperature, the 2-m temperature, the dry potential temperature, the water vapor mixing ratio, the wind speed, and direction) present a good agreement with observed data. In view of every upper-air and surface IOA2 values, there is only one disagreement value: for the 0800 LT wind direction at the 1000-hPa pressure level, probably induced by the transition time between nocturnal and diurnal conditions. The simulations allow us to complete the coarse descriptions of Bleuse and Bleuse (1997) and Brévignon (2003), which did not included a map distribution of the wind, skin temperature, cloud cover, and sensible heat flux for the whole archipelago. The three local wind regime areas (windward, inland, and leeward) described by these authors are retrieved in the model outputs, including the predominance of thermal and orographic effects, respectively over Grande-Terre Island and Basse-Terre Island.

Under STW ($Fr_m = 0.82$), at daytime and nighttime, island-scale circulations are driven by the orography. Over low lands (i.e., Grande-Terre) the convection is inhibited, the sky is clear, and a compact cloud cover develops on the mountains of Basse-Terre. The orographic effects predicted for adiabatic flow in section 2 drive the airflow; there is a weakly nonlinear regime at the mountain range of North Basse-Terre and wave breaking at the volcano of La Soufrière.

Under MTW ($Fr_m = 0.41$) and WTW ($Fr_m = 0.21$), the expected orographic effects are impacted by the thermal forcing. At daytime, the convection enhanced by the land–sea thermal contrast generates cloud lines and cloud clusters over the slopes of Basse-Terre. The marine airflow converges over lands. At nighttime, the strong radiative cooling induces weak diverging airflow circulations over Grande-Terre, whereas over Basse-Terre it induces a westerly katabatic flow linked with a windward dynamical blocking in the area of the volcano (expected in section 2). However, in the MTW case the Froude number has a greater value than in WTW case, which limits these particular nocturnal circulations for two reasons. First, the land breeze with offshore extension occurring during WTW is dynamically inhibited by the MTW trade wind strength. This trade wind speed is also sufficient to produce nocturnal orographic clouds that inhibit the radiative cooling. As a consequence the MTW katabatic flow is weaker than that of the WTW.

The WTW simulation allowed a better understanding of the nocturnal flow reversal, measured by D'Alexis et al. (2011) on the windward coast of Basse-Terre island. The model showed that this cold gravity current starts at 1800 LT from a diverging point located at 16.1221°N, 61.6591°W, and 566 m MSL. The katabatic wind flows successively to the areas of VER, ARN, and PCM. This reversed flow extends to Grande-Terre Island and confluences with land-breeze circulations over PCM (i.e., Le Petit Cul-de-Sac Marin). Between 0800 and 0900 LT, the radiative heating of the slopes stops the flow. The analysis of this simulated flow around the area of ARN indicates these main characteristics: a duration of 12 h, a maximum height of 250 m AGL with a return current at 400 m AGL, a mean wind speed of 2.4 m s^{-1}, and a maximum wind speed of 4.7 m s^{-1}.

This particular nocturnal flow occurring in the most densely populated area produces an important nocturnal pollution period due to industrial sources (e.g., the diesel power plants of the archipelago). To examine this flow more in detail at 100-m scale, the next numerical study will be performed using a coupling of WRF with a large-eddy simulation (WRF-LES) and a Computational Fluid Dynamics (CFD) software. The ARN observational dataset indicated that the katabatic flow was well simulated at this location. A new field campaign will be set up to have another comparison point. The meteorological weather station, previously placed on the ARN coast (D'Alexis et al. 2011) will be placed at the upstream point VER.

Acknowledgments. The weather-type classification and the observational data from RZT, MOU, GBD, and DES stations were obtained from the French Met Office (Météo France) thanks to Philippe Palany. The WRF simulations were computed on the Phoebus cluster [Scientific Computing Center of Région Centre (CCSC), University of Orléans] and the Orca cluster [Intensive Computing Center (C3I), University of the French West Indies and French Guiana]. The authors wish to thank Danièle Frison and Bernard Dhuicq who helped with the translation. The authors wish to pay tribute to the

memory of Bernard Dhuicq who died during the review period.

APPENDIX

Model Error Estimators

Statistical tools widely used in meteorological numerical studies, were developed by Willmott (1981) and Willmott and Matsuura (2005). Individual model-prediction errors are defined as $e_i = P_i - O_i$ ($i = 1, 2, \ldots, n$), where P_i and O_i are model predictions and in situ observations, respectively. The mean bias error is written as $\mathrm{MBE} = n^{-1}\sum_{i=1}^{n} e_i = \overline{P} - \overline{O}$. The mean absolute error is defined as $\mathrm{MAE} = n^{-1}\sum_{i=1}^{n} |e_i|$. The root-mean-square error is based on the sum of squared errors: $\mathrm{RMSE} = [n^{-1}\sum_{i=1}^{n} |e_i|^2]^{1/2}$. Willmott (1981) defined an index of agreement (IOA) as

$$\mathrm{IOA} = 1 - \frac{\sum_{i=1}^{n} |e_i|^2}{\sum_{i=1}^{n} [|P_i - \overline{O}| + |O_i - \overline{O}|]^2}, \qquad \text{(A1)}$$

with a lower limit of 0 and an upper limit of 1. Values greater than 0.5 are considered to be good. Willmott et al. (2012) developed a refined index of agreement (with the value range of [−1, 1]), logically related to increases and decreases in MAE. They expressed this new index as

$$\mathrm{IOA2} = \begin{cases} 1 - \dfrac{\sum_{i=1}^{n} |e_i|}{2\sum_{i=1}^{n} |O_i - \overline{O}|}, & \text{when} \quad \sum_{i=1}^{n} |e_i| \le 2\sum_{i=1}^{n} |O_i - \overline{O}| \\ \dfrac{2\sum_{i=1}^{n} |O_i - \overline{O}|}{\sum_{i=1}^{n} |e_i|} - 1, & \text{when} \quad \sum_{i=1}^{n} |e_i| > 2\sum_{i=1}^{n} |O_i - \overline{O}| \end{cases} . \qquad \text{(A2)}$$

According to Eq. (A2), a value of IOA2 of 0.5 indicates that the sum of error magnitudes is one-half of the sum of perfect-model-deviation and observed-deviation magnitudes. On the other hand, a value of IOA2 of −0.5 means that the sum of error magnitudes is twice the sum of the perfect-model-deviation and observed-deviation magnitudes.

REFERENCES

Bauer, M. H., G. J. Mayr, I. Vergeiner, and H. Pichler, 2000: Strongly nonlinear flow over and around a three-dimensional mountain as a function of the horizontal aspect ratio. *J. Atmos. Sci.,* **57,** 3971–3991.

Bleuse, P., and N. Bleuse, 1997: Quelques aspects du vent en Guadeloupe (Some features of wind in Guadeloupe). Tech. Rep., Météo-France, DIRAG, Service Régional de Guadeloupe, 22 pp.

Brévignon, C., 2003: *Atlas Climatique: l'Environnement Atmosphérique de la Guadeloupe, de Saint-Barthélémy et Saint-Martin (Climatic Atlas: Atmospheric Environment in Guadeloupe, Saint Barthélémy and Saint Martin).* Météo-France, Service Régional de Guadeloupe, 92 pp.

Carlis, D. L., Y.-L. Chen, and V. R. Morris, 2010: Numerical simulations of island-scale airflow over Maui and the Maui vortex under summer trade wind conditions. *Mon. Wea. Rev.,* **138,** 2706–2736.

Cécé, R., J.-F. Dorville, and D. Bernard, 2013: High resolution atmospheric and oceanic modelling: Impacts of Hurricane Dean over the Guadeloupe archipelago. *Proc. Caribbean Waves 2,* Gosier, Guadeloupe, LaRGE–UAG, 71–72.

Chen, F., and J. Dudhia, 2001: Coupling an advanced land surface-hydrology model with the Penn State–NCAR MM5 modeling system. Part I: Model implementation and sensitivity. *Mon. Wea. Rev.,* **129,** 569–585.

D'Alexis, C., 2011: Mesures expérimentales dans les basses couches de l'atmosphère tropicale insulaire (Guadeloupe): Micro-météorologie et composition chimique des masses d'air nocturnes en zone de mangrove [Experimental measurements in the insular tropical atmospheric boundary layer (Guadeloupe): Microscale meteorology and chemical composition of nocturnal air masses in mangrove area.] Ph.D. thesis, Université des Antilles et de la Guyane, Pointe-à-Pitre, Guadeloupe, 213 pp.

——, A. Abouna, H. Berthelot, and D. Bernard, 2011: Characteristics of nocturnal breezes in the Windward Islands in the Southeastern Caribbean: Structure and nighttime regimes. *J. Caribbean Acad. Sci.,* **5** (2). [Available online at http://ojs.mona.uwi.edu/index.php/cas/issue/view/281.]

De Souza, R. L., 1972: A study of atmospheric flow over a tropical island. Ph.D. thesis, Florida State University, 204 pp.

Dudhia, J., 1989: Numerical study of convection observed during the winter monsoon experiment using a mesoscale two-dimensional model. *J. Atmos. Sci.,* **46,** 3077–3107.

Feng, J., and Y.-L. Chen, 1998: Evolution of katabatic flow on the island of Hawaii on 10 August 1990. *Mon. Wea. Rev.,* **126,** 2185–2199.

Hong, S.-Y., and J.-O. J. Lim, 2006: The Kain-Fritsch convective parameterization: An update. *J. Korean Meteor. Soc.,* **42** (2), 129–151.

——, Y. Noh, and J. Dudhia, 2006: A new vertical diffusion package with an explicit treatment of entrainment processes. *Mon. Wea. Rev.,* **134,** 2318–2341.

Hu, X.-M., J. W. Nielsen-Gammon, and F. Zhang, 2010: Evaluation of three planetary boundary layer schemes in the WRF model. *J. Appl. Meteor. Climatol.,* **49,** 1831–1844.

Jury, M. R., S. Chiao, and E. W. Harmsen, 2009: Mesoscale structure of trade wind convection over Puerto Rico: Composite observations and numerical simulation. *Bound.-Layer Meteor.,* **132,** 289–313, doi:10.1007/s10546-009-9393-3.

Kain, J. S., 2004: The Kain–Fritsch convective parameterization: An update. *J. Appl. Meteor.,* **43,** 170–181.

Lefèvre, J., P. Marchesiello, N. C. Jourdain, C. Menkes, and A. Leroy, 2010: Weather regimes and orographic circulation around New Caledonia. *Mar. Pollut. Bull.,* **61,** 413–431.

Lesouëf, D., F. Gheusi, R. Delmas, and J. Escobar, 2011: Numerical simulations of local circulations and pollution transport over Reunion Island. *Ann. Geophys.,* **29,** 53–69.

Mahrer, Y., and R. A. Pielke, 1976: Numerical simulation of the airflow over Barbados. *Mon. Wea. Rev.,* **104,** 1392–1402.

Malkus, J. S., 1955: The effects of a large island upon the trade-wind air stream. *Quart. J. Roy. Meteor. Soc.,* **81** (350), 538–550.

Matthews, S., J. M. Hacker, J. Cole, J. Hare, C. N. Long, and R. M. Reynolds, 2007: Modification of the atmospheric boundary layer by a small island: Observations from Nauru. *Mon. Wea. Rev.,* **135,** 891–905.

Mlawer, E. J., S. J. Taubman, P. D. Brown, M. J. Iacono, and S. A. Clough, 1997: Radiative transfer for inhomogeneous atmosphere: RRTM, a validated correlated-k model for the longwave. *J. Geophys. Res.,* **102** (D14), 16 663–16 682.

Morvan, K., 2011: Réalisation d'une climatologie et d'une classification en type de temps sur les Petites Antilles et la Guyane (Achievement of a climatology and a classification of weather types in the French Lesser Antilles and French Guiana). M.S. thesis, Université des Antilles et de la Guyane, 147 pp.

Nguyen, H. V., Y.-L. Chen, and F. Fujioka, 2010: Numerical simulations of island effects on airflow and weather during the summer over the island of Oahu. *Mon. Wea. Rev.,* **138,** 2253–2280.

Oliphant, A. J., A. P. Sturman, and N. J. Tapper, 2001: The evolution and structure of a tropical island sea/land-breeze system, northern Australia. *Meteor. Atmos. Phys.,* **78,** 45–59.

Reisner, J. M., and P. K. Smolarkiewicz, 1994: Thermally forced low Froude number flow past three-dimensional obstacles. *J. Atmos. Sci.,* **51,** 117–133.

Savijrvi, H., and S. Matthews, 2004: Flow over small heat islands: A numerical sensitivity study. *J. Atmos. Sci.,* **61,** 859–868.

Skamarock, W. C., and Coauthors, 2008: A description of the Advanced Research WRF version 3. Tech. Rep. NCAR/TN-475+STR, National Center for Atmospheric Research, 125 pp. [Available online at http://www.mmm.ucar.edu/wrf/users/docs/arw_v3.pdf.]

Smith, R. B., 1989: Hydrostatic airflow over mountains. *Advances in Geophysics,* Vol. 31, Academic Press, 59–81.

——, and S. Grønås, 1993: Stagnation points and bifurcation in 3-D mountain airflow. *Tellus,* **45A,** 28–43.

——, and V. Grubiac, 1993: Aerial observations of Hawaii's wake. *J. Atmos. Sci.,* **50,** 3728–3750.

——, A. C. Gleason, and P. A. Gluhosky, 1997: The wake of St. Vincent. *J. Atmos. Sci.,* **54,** 606–623.

——, and Coauthors, 2012: Orographic precipitation in the tropics: The Dominica experiment. *Bull. Amer. Meteor. Soc.,* **93,** 1567–1579.

Smolarkiewicz, P. K., and R. Rotuno, 1989: Low Froude number flow past three-dimensional obstacles. Part I: Baroclinically generated lee vortices. *J. Atmos. Sci.,* **46,** 1154–1164.

Willmott, C. J., 1981: On the validation of models. *Phys. Geogr.,* **2** (2), 184–194.

——, and K. Matsuura, 2005: Advantages of the mean absolute error (MAE) over the root mean square error (RMSE) in assessing average model performance. *Climate Res.,* **30,** 79–82.

——, S. M. Robeson, and K. Matsuura, 2012: A refined index of model performance. *Int. J. Climatol.,* **32,** 2088–2094, doi:10.1002/joc.2419.

Yang, Y., and Y.-L. Chen, 2005: Numerical simulations of the island-induced circulations over the island of Hawaii during HaRP. *Mon. Wea. Rev.,* **133,** 3693–3713.